

See discussions, stats, and author profiles for this publication at: <https://www.researchgate.net/publication/328698185>

Fatigue Damage Mitigation of Offshore Wind Turbines under Real Wind and Wave Conditions

Article in *Engineering Structures* · November 2018

DOI: 10.1016/j.engstruct.2018.10.053

CITATIONS

7

READS

353

2 authors:



Chao Sun

Louisiana State University

27 PUBLICATIONS 268 CITATIONS

[SEE PROFILE](#)



Vahid Jahangiri

Louisiana State University

10 PUBLICATIONS 64 CITATIONS

[SEE PROFILE](#)

Some of the authors of this publication are also working on these related projects:



Vibration Control of Monopile Offshore Wind Turbine [View project](#)



Concrete Constitutive Law Modeling Using CT Technique [View project](#)

Fatigue Damage Mitigation of Offshore Wind Turbines under Real Wind and Wave Conditions

Chao Sun*, Vahid Jahangiri,

Department of Civil and Environmental Engineering, Louisiana State University, Baton Rouge, LA 70803, USA

Abstract

Offshore wind turbines (OWTs) subjected to combined wind and wave loadings experience excessive vibrations which will increase fatigue loadings on the structure and reduce the fatigue life. In this paper, a three-dimensional pendulum tuned mass damper (3d-PTMD) is attached to the OWT to mitigate the bi-directional vibrations resulting from wind-wave misalignment so as to increase the fatigue life. An analytical model of the offshore wind turbine coupled with the 3d-PTMD is established using the Euler-Lagrangian equation. To predict long-term metocean condition, a statistical analysis for different properties of wind and wave loading such as, wind-wave misalignment, significant wave height and wind velocity is carried out. The aerodynamic wind loading is calculated using the blade element method and the wave loading is computed using the JONSWAP wave spectrum and Morison equation. Dual linear tuned mass dampers (TMDs) deployed in the side-side and fore-aft directions are used for comparison. The NREL monopile 5 MW baseline wind turbine is used to examine the performance of 3d-PTMD in a realistic metocean condition. The fatigue damage is estimated based on the rain-flow cycle counting method and Miner's rule. Results indicate that the 3d-PTMD can increase the wind turbine tower fatigue life by more than 50% in comparison with the dual TMDs.

Keywords: Offshore wind turbines; pendulum tuned mass damper; wind-wave misalignment; fatigue damage mitigation

1. Introduction

Increasing demand for renewable energy has led a significant growth in wind energy production. Steadier and higher wind speed, less space limitation and lower visual and noise pollutions in the marine area render offshore wind turbines (OWTs) more attractive than their onshore counterparts. However, because of the severe marine conditions such as strong wind, wave and storm surge, the OWTs suffer from excessive vibrations which will cause severe fatigue damage of the structure, reducing the structural service life and increasing the operation and maintenance cost.

To mitigate the wind and wave induced fatigue damage, structural vibration control which has been actively studied and successfully applied in protecting civil structures is being investigated to protect the OWTs. Structural vibration control generally falls into three primary categories: passive control, active control and semi-active control. Passive control strategy which is easy to apply has attracted active research effort. Colwell and Basu [1] studied the vibration mitigation of the monopile offshore wind turbine using a tuned liquid column damper (TLCD). It was found that the TLCD can increase the tower fatigue life. Lackner and Rotea [2] used two independent linear tuned mass dampers (TMDs) located in the nacelle of the OWT to control the vibrations in both side-side and fore-aft directions. The authors found that the dual passive TMDs can reduce the structural response in both directions. Dinh and Basu [3] investigated the use of multiple TMDs to mitigate the vibration of a spar-type OWT. Research results show that the multiple TMDs are more effective than a single TMD in reducing the structural responses.

Although passive control strategies are effective within the targeted frequency range, they might lose their effectiveness because of environmental and system variations. To overcome this issue, Lackner and Rotea [4] investigated active control for a floating barge-type wind turbine. It was found that active control is more effective than passive control in mitigating the structural vibrations. Staino et al. [5] used active tendons mounted inside the blade to control the edgewise vibration of wind turbine blades. It was concluded that the proposed active control scheme can mitigate the vibrations of the wind turbine blades. Fitzgerald et al. [6] used an active tuned mass damper to mitigate the in-plane vibration of the blades. The authors found that active tuned mass damper can provide better reduction than passive tuned mass damper.

In comparison with active control, semi-active control which can provide comparable mitigation effect yet requires orders of magnitude smaller input energy is studied to mitigate the OWTs vibrations considering environmental and system variations. Sun [7,8] introduced a semi-active TMD (STMD) with tunable natural frequency and damping ratio to control the monopile OWT vibrations. It was found that with damage presence, the passive TMD becomes off-tuned and loses its effectiveness while the STMD remains effective in mitigating the structural response. Huang and Arrigan et al. [9,10] studied the use of an STMD in mitigating the vibrations of wind turbine blades. It was found that the STMD can reduce the vibrations of the blades in a time-variant environmental condition. Dinh et al. [11] used an STMD and placed it in the wind turbine blades, nacelle and platform. It was observed that the STMD is more effective than the passive TMD when subjected to a time-variant cable tension, rotor speed and blade stiffness.

According to recorded metocean data, wind and wave directions are often misaligned [12]. The wind-wave misalignment causes the OWT to vibrate in both fore-aft and side-side directions. Stewart and Lackner [12] used dual linear TMDs to control the bi-directional structural vibrations. It was found that the dual TMDs reduce the tower fore-aft fatigue load by around 5% and the side-side fatigue load by up to 40%. However, several limitations exist in this approach. First, the total TMD mass and the relative angle between two TMDs are correlated with the probabilistic distribution of the magnitude and directionality of the external loading which can be challenging for the designers. Furthermore, the dual TMDs require more space and larger mass and more cost for installation and maintenance. Hence, using a tuned mass damper which is capable of mitigating the bi-directional vibrations simultaneously is desired. Sun et al. [13,14] studied the planar adaptive PTMDs whose natural frequency and damping properties can be retuned to account for environmental and structural variations. It was shown that the adaptive PTMD is able to reduce the vibration and avoid the occurrence of bifurcation in nonlinear systems. On the basis of [13,14], the authors of the present paper proposed a three dimensional pendulum tuned mass damper (3d-PTMD) to mitigate the bi-directional vibration of the OWTs [15]. Research findings show that the 3d-PTMD outperforms the dual linear TMDs in mitigating the bi-directional vibration. However, the performance of the proposed 3d-PTMD in mitigating the fatigue damage of the OWTs under real recorded metocean data has not been evaluated.

It is reported that a new wind farm with monopile fixed-bottom OWTs in US is under development [16] at a location where the latitude is 38.547° and longitude is -74.667° . Therefore, the present study will attempt to mitigate the fatigue damage of monopile OWTs under real metocean conditions recorded at the location of the new wind farm by employing the proposed 3d-PTMD in [15]. A fully coupled three-dimensional model of the monopile OWT with a 3d-PTMD is established using Euler-Lagrangian equation. The aerodynamic wind loading is calculated using blade element method and the wave loading is computed using Morison equation. To capture the

statistical characteristics of the realistic metocean data, the probabilistic distribution of the wind speed, significant wave height and misalignment angle is analyzed. The joint probability density functions of wind speed, significant wave height and misalignment angle are determined based on which the fatigue damage of the structure is estimated using rain-flow counting method. The performance of the 3d-PTMD in mitigating the fatigue damage is evaluated and compared to the dual linear TMDs. Results show that the 3d-PTMD outperforms the linear dual TMDs in mitigating the tower's fatigue damage under real metocean conditions.

2. Establishment of the Analytical Model

A fully coupled three-dimensional model for a monopile OWT with a 3d-PTMD attached to it, is established using Euler-Lagrangian equation. Fig. 1 illustrates the schematic model of the OWT with a 3d-PTMD placed in the nacelle. Totally, the coupled system contains 14 degrees of freedom (DOF) with $q_1 \sim q_6$ representing the blade in-plane and out-of-plane coordinate, $q_7 \sim q_8$ representing the nacelle fore-aft and side-side coordinate, $q_9 \sim q_{12}$ representing the translational and rotational coordinates of the foundation and $q_{13} \sim q_{14}$ representing the relative coordinate of the 3d-PTMD with respect to the nacelle. The soil effects in this paper is modeled with a pair of springs and dash-pots. The stiffness coefficient of soil effects for translational coordinates is represented by k_x, k_y and rotational springs with coefficients of $k_{x\varphi}, k_{y\varphi}$. Similarly, the damping coefficients for translational coordinates is represented by c_x, c_y and rotational dampers with coefficients of $c_{x\varphi}$ and $c_{y\varphi}$. In Fig. 1(a), wind-wave misalignment is considered and denoted as β . As shown in Fig. 1 (b), a local coordinate system $o_r - x_r, y_r, z_r$ originating at the rest position of the pendulum is defined where the 3d-PTMD will move along a spherical surface when the nacelle moves in the fore-aft and side-side directions. Figs. 1 (c) and (d) show the pendulum motion in the fore-aft and side-side directions where c_{px} and c_{py} are the damping coefficient of the damper in x_r and y_r directions.

The Euler-Lagrangian equation is used to establish the equations of motion of the monopile OWT coupled with 3d-PTMD. The equation is expressed as follows:

$$\frac{d}{dt} \frac{\partial T(t, \tilde{q}(t), \dot{\tilde{q}}(t))}{\partial \dot{q}_i(t)} - \frac{\partial T(t, \tilde{q}(t), \dot{\tilde{q}}(t))}{\partial q_i(t)} + \frac{\partial V(t, \tilde{q}(t))}{\partial q_i(t)} = Q_i(t) \quad (1)$$

where T and V are the kinetic and potential energy, $\tilde{q}(t)$ is the generalized coordinates vector, $Q_i(t)$ is the generalized force corresponding to the i^{th} component of $\tilde{q}(t)$.

The absolute displacement of the nacelle in the fore-aft direction u_{nac}^{fa} and the side-side direction u_{nac}^{ss} can be expressed as:

$$\begin{aligned} u_{nac}^{fa} &= q_7 + q_9 + h \tan(q_{10}) \approx q_7 + q_9 + h q_{10} \\ u_{nac}^{ss} &= q_8 + q_{11} + h \tan(q_{12}) \approx q_8 + q_{11} + h q_{12} \end{aligned} \quad (2)$$

By taking the derivative of Eq. (2), the absolute velocity in both directions can be found and the resultant absolute velocity of the nacelle v_{nac} , can be determined as:

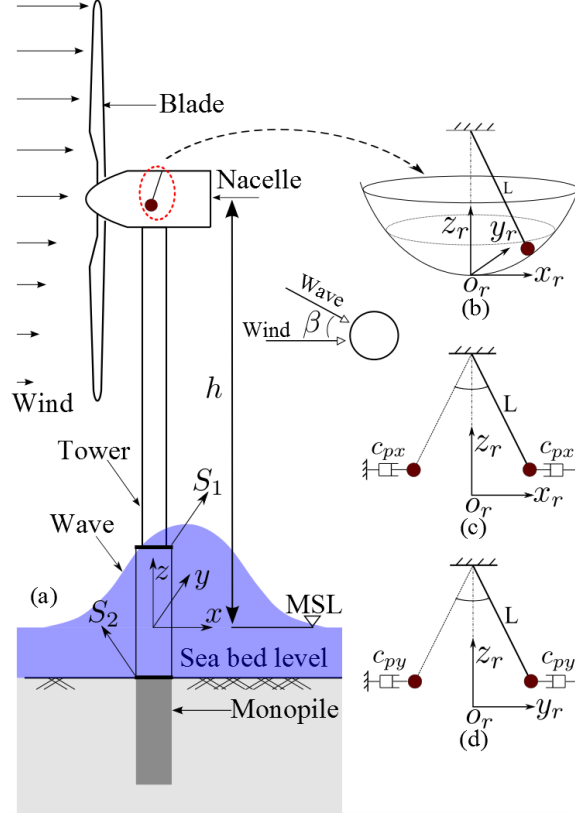


Fig. 1. Monopile OWT coupled with a 3d-PTMD subjected to wind-wave loadings. (a): original model; (b): configuration of the PTMD; (c): pendulum in xz plane; (d): pendulum in yz plane.

$$\begin{aligned} v_{nac}^{fa} &= \dot{q}_7 + \dot{q}_9 + h\dot{q}_{10} \\ v_{nac}^{ss} &= \dot{q}_8 + \dot{q}_{11} + h\dot{q}_{12} \end{aligned} \quad (3)$$

The blades rotating speed is Ω and the azimuth angle is shown with $\psi_j(t)$ of the j^{th} blade can be expressed as follows:

$$\psi_j = \Omega t + \frac{2\pi}{3}(j-1), \quad j = 1, 2, 3 \quad (4)$$

The absolute coordinate of the PTMD can be expressed as:

$$x_p = u_{nac}^{ss} + x_r, \quad y_p = u_{nac}^{fa} + y_r, \quad z_p = L - \sqrt{L^2 - x_r^2 - y_r^2} \quad (5)$$

The kinetic energy of the pendulum is determined as follows:

$$\begin{aligned} T_p &= \frac{1}{2} m_p [\dot{x}_p^2 + \dot{y}_p^2 + \dot{z}_p^2] \\ &= \frac{1}{2} m_p \left[(v_{nac}^{ss})^2 + (v_{nac}^{fa})^2 + 2v_{nac}^{ss}\dot{x}_r + 2v_{nac}^{fa}\dot{y}_r + \dot{x}_r^2 + \dot{y}_r^2 + \frac{\sqrt{L^2 - x_r^2 - y_r^2}}{(v_{nac}^{ss}\dot{x}_r + v_{nac}^{fa}\dot{y}_r)^2} \right] \end{aligned} \quad (6)$$

where m_p is the pendulum mass.

Finally, the kinetic energy of the wind turbine system with coupled 3d-PTMD can be expressed as:

$$T = \frac{1}{2} \sum_{j=1}^3 \int_0^R \bar{m} v_{bj}^2(r, t) dr + \frac{1}{2} M_{nac} v_{nac}^2 + \frac{1}{2} \int_0^h \bar{M} v_{tow}^2 dz + \frac{1}{2} M_f [\dot{q}_9^2(t) + \dot{q}_{11}^2(t)] + \frac{1}{2} I_f [\dot{q}_{10}^2(t) + \dot{q}_{12}^2(t)] + T_p \quad (7)$$

where M_{nac} is the mass of the nacelle including the hub, M_f and I_f are the foundation mass and moment of inertia, \bar{m} and \bar{M} are the mass density per length of the blade and the tower. Parameters v_{bj} and v_{tow} are the absolute velocity of the blade and tower respectively which are determined in Ref. [7].

Also, the potential energy of the pendulum is expressed as follows:

$$V_p = m_p g (L - \sqrt{L^2 - x_r^2 - y_r^2}) \quad (8)$$

Therefore, the total potential energy V of the wind turbine system is:

$$V = V_b + \frac{1}{2} k_t^{fa} q_7^2(t) + \frac{1}{2} k_t^{ss} q_8^2(t) + \frac{1}{2} k_x q_9^2(t) + \frac{1}{2} k_y q_{11}^2(t) + \frac{1}{2} k_{x\varphi} q_{10}^2(t) + \frac{1}{2} k_{y\varphi} q_{12}^2(t) + V_p \quad (9)$$

where, V_b is the potential energy of the blades which can be defined in Ref. [7], k_t^{fa} and k_t^{ss} are the fore-aft and side-side stiffness of the tower.

By substituting Eqs. (7) and (9) into Eq. (1), the equations of motion are derived and expressed in a matrix form as:

$$\tilde{M} \ddot{\tilde{q}} + \tilde{C} \dot{\tilde{q}} + \tilde{K} \tilde{q} = \tilde{Q}_{wind} + \tilde{Q}_{wv} + \tilde{F} \quad (10)$$

where \tilde{M} , \tilde{C} and \tilde{K} are the system mass, damping and stiffness matrices with a dimension of 14×14 . Variables \tilde{Q}_{wind} and \tilde{Q}_{wv} are the generalized force vectors corresponding to wind and wave loadings which can be found in next sections. It should be noted that since \tilde{M} , \tilde{C} and \tilde{K} are time variant, Eq. (10) is nonlinear. Parameter \tilde{F} is the generalized force caused by the nonlinearity of the pendulum. Detailed mathematical formulas of \tilde{M} , \tilde{C} and \tilde{K} and \tilde{F} can be found in Ref. [15].

3. Wind Loading

This section presents the derivation of the generalized force vector \tilde{Q}_{wind} corresponding to the wind loading based on the Principals of Virtual Work. Wind speed time-history is generated for each of the blade element via a three-dimensional wind field model. The aerodynamic loading is calculated based on the BEM method.

Wind velocity $v(z, t)$ can be represented by the summation of a constant mean velocity $\bar{v}(z)$ and a turbulent component $\tilde{v}(z, t)$, i.e.

$$v(z, t) = \bar{v}(z) + \tilde{v}(z, t) \quad (11)$$

In the present study, the logarithmic wind profile is adopted to calculate the mean velocity $\bar{v}(z)$, i.e.

$$\bar{v}(z) = V_{ref} \frac{\log(z / z_0)}{\log(H_{ref} / z_0)} \quad (12)$$

where V_{ref} is the mean velocity at the reference height $H_{ref} = 90m$. Parameter z_0 is the length of roughness and its value is $z_0 = 0.03$.

The turbulent component of wind velocity $\tilde{v}(t)$ is computed using the IEC Kaimal spectral model which is described by the following equations:

$$S_v(f) = \frac{4I^2 L_c}{(1 + 6fL_c / \bar{v})^{5/3}} \quad (13)$$

where $S_v(f)$ is the power spectral density function, f is the wind frequency in Hz , I is the wind turbulence intensity and L_c is an integral scale parameter.

To account for the spatial dependency of wind velocity $\tilde{v}(z, t)$ at different points, the cross spectra between two points i and j are defined as:

$$S_{ij}(f) = Coh(i, j; f) \sqrt{S_{ii}(f) S_{jj}(f)} \quad (14)$$

where S_{ij} is the cross spectra, S_{ii} and S_{jj} are the auto spectra at points i and j , respectively. Referring to the IEC spectral mode [17], the spatial coherence function is given as:

$$Coh(i, j; f) = \exp \left(-a \sqrt{\left(\frac{fL}{\bar{v}_{hub}} \right)^2 + \left(\frac{0.12L}{L_c} \right)^2} \right) \quad (15)$$

Based on Eqs. (12) to (15), a three-dimensional wind field profile represented by 31×31 velocity grids covering the domain of the rotor disk is generated using the TurbSim program [17] as shown in Fig. 2 where the wind velocity is mapped onto the rotating blades. Wind shear power law with an exponent of 0.1 is used to describe the mean wind velocity Matlab code has been developed to map the full wind field profile onto each span station of the rotating blades. As an illustration, wind velocity time history at the center of the tip element of blade 1 is shown in Fig. 3 where the mean wind velocity $\bar{v} = 18m/s$ and the turbulence intensity is $TI = 10\%$.

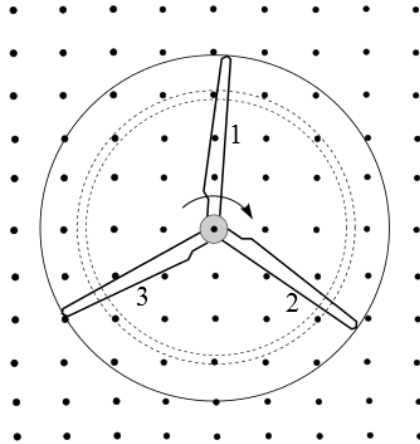


Fig. 2. Three dimensional wind profile and the rotating blades

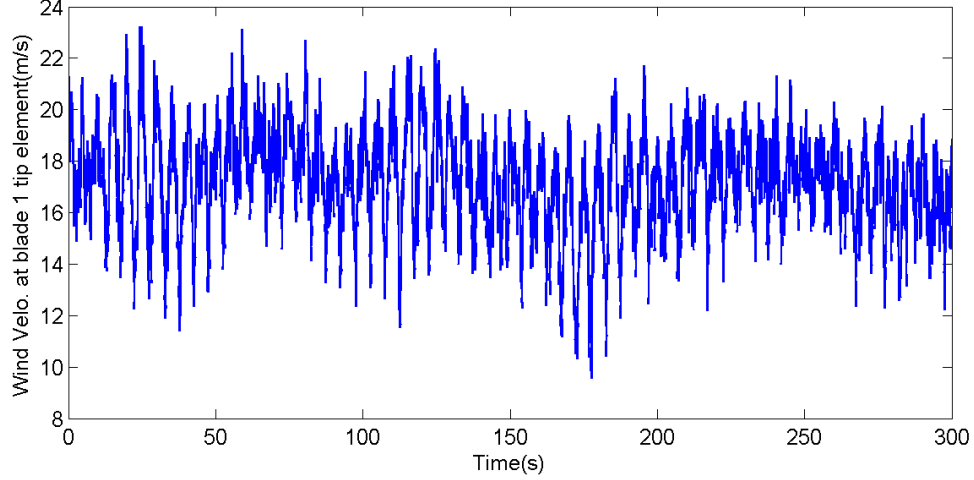


Fig. 3. Wind velocity at the tip element of blade 1 ($\bar{v} = 18m / s$ at hub height and $TI = 10\%$).

In the present study, the Blade Element Momentum (BEM) theory is used to estimate the aerodynamic loading acting on the rotating blades. Time series of the aerodynamic loading are computed based on the momentum theory, the blade characteristics and the operational conditions. The input parameters include the rotor geometry, wind speed and the blade rotational [18].

Fig. 4 illustrates a general turbine blade discretized into N elements for BEM analysis where R is the rotor radius and Ω is the rotation velocity. It is assumed in the BEM theory that no radial dependency exists along the blade span and thus the element can be analyzed independently via performing the momentum theory. In Fig. 4, the i^{th} blade element at a distance r is detailed where dr is the element span length and $c(r)$ is the chord length at the element mid-span.

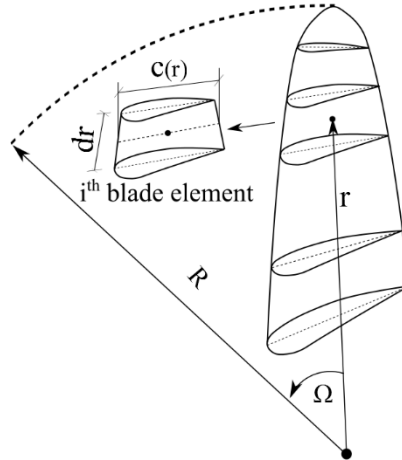


Fig. 4. Turbine blade discretized into N blade elements for BEM analysis

An arbitrary blade element experiencing local velocities and aerodynamic loading is illustrated in Fig. 5. The relative wind velocity V_{rel} can be expressed by combining the axial velocity $v(1 - a)$ and the tangential velocity $\Omega r(1 + a')$ as:

$$V_{rel} = \sqrt{[v(1 - a)^2] + [\Omega r(1 + a')]^2} \quad (16)$$

where a and a' are the axial velocity and tangential velocity induction factors.

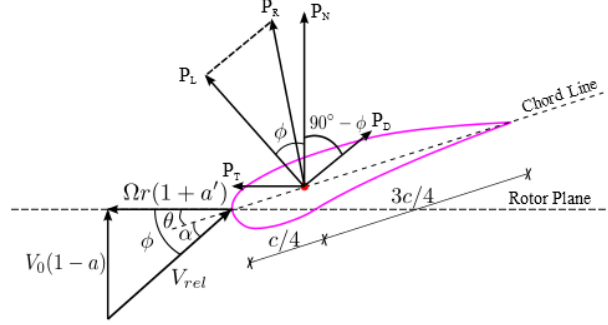


Fig. 5. Blade element section subjected to local velocity and aerodynamic loading

The flow angle ϕ can be calculated by

$$\phi = \tan^{-1} \frac{v(1-a)}{\Omega r(1+a')} \quad (17)$$

The attack angle α between the relative velocity V_{rel} and chord line is obtained as:

$$\alpha = \phi - \theta \quad (18)$$

where θ is the summation of the pitch angle and the twist which is predetermined by the airfoil.

The normal and tangential forces P_N and P_T can be calculated as:

$$P_N = \frac{1}{2} \rho V_{rel}^2 c C_N, \quad P_T = \frac{1}{2} \rho V_{rel}^2 c C_T \quad (19)$$

where ρ is the air density and c is the chord length. Parameters C_N and C_T are the normal and the tangential coefficients respectively which can be calculated as: $C_N = \cos \phi C_l + \sin \phi C_d$ and $C_T = \sin \phi C_l - \cos \phi C_d$. The lift and drag coefficients shown with C_l and C_d can be determined from the airfoil data.

Eqs. (15) through (19) demonstrate the primary procedure to calculate the aerodynamic load. In real application, a and a' are unknown and need to be determined via iterations. Matlab code has been developed to calculate the time series of P_N and P_T in the present study based on the algorithm proposed in [18]. Prandtl's tip loss factor and Glauert correction are considered in the Matlab code. Next the Principle of Virtual Work is applied to calculate the generalized aerodynamic load.

Under P_N and P_T , the virtual work δW_{wl} done by external wind load is:

$$\delta W_{wl} = \sum_{j=1}^3 \left\{ \int_0^R P_{Tj}(r, t) [\phi_{1e} \delta q_j + \delta u_{nac}^{ss} \cos(\psi_j)] dr + \int_0^R P_{Nj}(r, t) [\phi_{1f} \delta q_{j+3} + \delta u_{nac}^{fa}] dr \right\} \quad (20)$$

where $P_{Tj}(r, t)$ and $P_{Nj}(r, t)$ denote the tangential and normal wind loading intensity per unit length on the j^{th} blade.

In terms of the principles of work and energy, the generalized force Q_j can be determined as:

$$Q_j = \frac{\partial(\delta W_{wl})}{\partial(\delta q_j)} \quad (21)$$

Substituting Eq. (20) into Eq. (21) yields the wind induced generalized forces:

$$\begin{aligned} Q_{j,wind} &= \int_0^R P_{Tj}(r,t) \phi_{1e} dr, \quad Q_{j+3,wind} = \int_0^R P_{Nj}(r,t) \phi_{1f} dr, \quad j = 1, 2, 3 \\ Q_{7,wind} &= \sum_{j=1}^3 \int_0^R P_{Nj}(r,t) dr, \quad Q_{8,wind} = \sum_{j=1}^3 \int_0^R P_{Tj}(r,t) dr \cos(\psi_j) \\ Q_{9,wind} &= Q_{7,wind}, \quad Q_{10,wind} = h Q_{7,wind}, \quad Q_{11,wind} = Q_{8,wind}, \quad Q_{12,wind} = h Q_{8,wind} \end{aligned} \quad (22)$$

It is noted that the wind loading acting on the tower is relatively small as compared to that on the blade and thus is ignored. MATLAB codes have been developed to calculate the time series of the aerodynamic loading based on Eqs. (16) ~ (22) in the present study. Prandtl's tip loss factor and Glauert correction are considered in the MATLAB code.

4. Wave Loading

This section presents the derivation of the generalized force vector \tilde{Q}_{uv} corresponding to the wave loading based on the Principals of Virtual Work. Linear wave and the strip theory are used to calculate the wave loading.

Wave loading on circular cylindrical structural members of fixed offshore structures can be estimated using Morison's equation [19]. For the monopile offshore wind turbine, the horizontal force dF acting on a strip of length dz can be written as:

$$dF = \frac{\pi D^2}{4} C_M \rho i dz + \frac{\rho}{2} C_D D u |u| dz \quad (23)$$

where C_M and C_D are the mass and drag coefficients ($C_M = 1.0$ and $C_D = 1.2$ are adopted in the present paper); ρ is water density (1025 kg/m^3), D is the diameter of the tower and the monopile; i and u are the wave induced horizontal acceleration and velocity of fluid particles.

In terms of Ref. [20] JONSWAP spectrum as listed in Eq. (24) is used to generate wave time histories.

$$S(f) = 0.3125 H_s^2 T_p \left(\frac{f}{f_p} \right)^5 \exp \left[-\frac{5}{4} \left(\frac{f}{f_p} \right)^4 \right] (1 - 0.287 \ln \gamma) \gamma^{\exp \left[\frac{(\omega - \omega_p)^2}{2\sigma^2 \omega_p^2} \right]} \quad (24)$$

where T_p is the wave period, H_s is the significant wave height, $f_p = \frac{1}{T_p}$, $\sigma = 0.07$ for $f \leq f_p$,

$\sigma = 0.09$ for $f > f_p$. Variable γ is the JONSWAP peakedness parameter[20]:

$$\gamma = \begin{cases} 5 & T_p / \sqrt{H_s} \leq 3.6 \\ \exp(5.75 - 1.15 T_p / \sqrt{H_s}) & 3.6 < T_p / \sqrt{H_s} \leq 5.0 \\ 1 & T_p / \sqrt{H_s} > 5.0 \end{cases} \quad (25)$$

Based on the spectrum representation method, the wave elevation $\eta(t)$, the fluid particle velocity u and the acceleration \dot{u} can be expressed as follows:

$$\eta(t) = \sum_{j=1}^N A_j \sin(\omega_j t - k_j x + \phi_j) \quad (26)$$

$$A_j = \sqrt{2S(\omega_j)\Delta\omega} \quad (27)$$

$$u = \sum_{j=1}^N \omega_j A_j \frac{\cosh[k(z + d_w)]}{T_\omega \sinh(kd_w)} \sin(\omega_j t - k_j x + \phi_j) \quad (28)$$

$$\dot{u} = \sum_{j=1}^N \omega_j^2 A_j \frac{\cosh[k(z + d_w)]}{T_\omega \sinh(kd_w)} \cos(\omega_j t - k_j x + \phi_j) \quad (29)$$

where k is the wave number in m^{-1} , ω is wave frequency in rad / sec , ϕ_j is a random phase angle uniformly distributed from 0 to 2π , d_w is the water depth, T_ω is the wave period and z is the vertical ordinate from mean water level.

Given water depth d_w , the parameters ω and k are related by the dispersion equation [20]:

$$k \tanh kd_w = \omega^2 / g \quad (30)$$

Hence, for any given water depth d_w , the wave number k can be determined via solving Eq. (30). Virtual work δW_{ww} done by the wave load along virtual displacement δu_{tow} of the tower can be written as:

$$\delta W_{ww} = \int_0^\eta dF \delta u_{tow} = \int_0^\eta dF [\phi_{1t}(\cos \beta \delta q_7 + \sin \beta \delta q_7) + \cos \beta (\delta q_9 + z \delta_{10}) + \sin \beta (\delta q_{11} + z \delta q_{12})] \quad (31)$$

Substituting Eq. (31) into Eq. (21) yields the generalized forces corresponding to wave:

$$\begin{cases} Q_{7,wave} = \cos \beta F_{wv,1}, & Q_{8,wave} = \sin \beta F_{wv,1} \\ Q_{9,wave} = \cos \beta F_{wv,2}, & Q_{10,wave} = \sin \beta F_{wv,2} \\ Q_{11,wave} = \cos \beta F_{wv,3}, & Q_{12,wave} = \sin \beta F_{wv,3} \end{cases} \quad (32)$$

where

$$\begin{aligned} F_{wv,1} &= \int_{-d_w}^{\eta(t)} \phi_{1t}(z) dF = \sum_{i=1}^{N_z} \phi_{1t}(z_i) \left[\frac{\rho \pi D^2(z_i)}{4} C_M \dot{u}(z_i, t) \Delta z + \frac{\rho}{2} C_D D(z_i) u(z_i, t) |u(z_i, t)| \Delta z \right] \\ F_{wv,2} &= \int_{-d_w}^{\eta(t)} dF = \sum_{i=1}^{N_z} \left[\frac{\rho \pi D^2(z_i)}{4} C_M \dot{u}(z_i, t) \Delta z + \frac{\rho}{2} C_D D(z_i) u(z_i, t) |u(z_i, t)| \Delta z \right] \\ F_{wv,3} &= \int_{-d_w}^{\eta(t)} z dF = \sum_{i=1}^{N_z} z_i \left[\frac{\rho \pi D^2(z_i)}{4} C_M \dot{u}(z_i, t) \Delta z + \frac{\rho}{2} C_D D(z_i) u(z_i, t) |u(z_i, t)| \Delta z \right] \end{aligned}$$

N_z represents the number of segments that the wetted portion of the tower is divided, parameter Δz denotes the segment length.

MATLAB codes have been developed to calculate the hydrodynamic loading based on Eqs. (23) ~ (32).

5. Wind and wave data

As mentioned in the Introduction, the Skipjack project with 15 monopile OWTs is under planning and will be constructed in the upcoming few years at a location where the latitude is 38.547° and longitude is -74.667° [16]. To evaluate the performance of the 3d-PTMD in mitigating the fatigue damage of the OWTs to be constructed, real metocean conditions recorded at this location are considered. The satellite map and the location of this station is shown in Fig. 6 where the raw data from station 44009 is downloaded from the National Data Buoy Center website[21]. In this study, 25 years' historical data is used. The downloaded raw data includes wind and wave directions, wind speed, wave period and significant wave height. Due to sensor malfunctions, some errors observed in the raw data are deleted from the original data.

The anemometer is located 5 m above the site elevation and the wind speed is captured accordingly. It is required to determine the wind speed at the hub height (90m). In this regard, wind shear power law with an exponent of 0.1 is used to extrapolate the wind speed at 90 meters. The cut-in and cut-out wind speeds are 3 m/s and 25 m/s respectively. The wind speeds more than the cut-out and less than the cut-in values are omitted from the data.

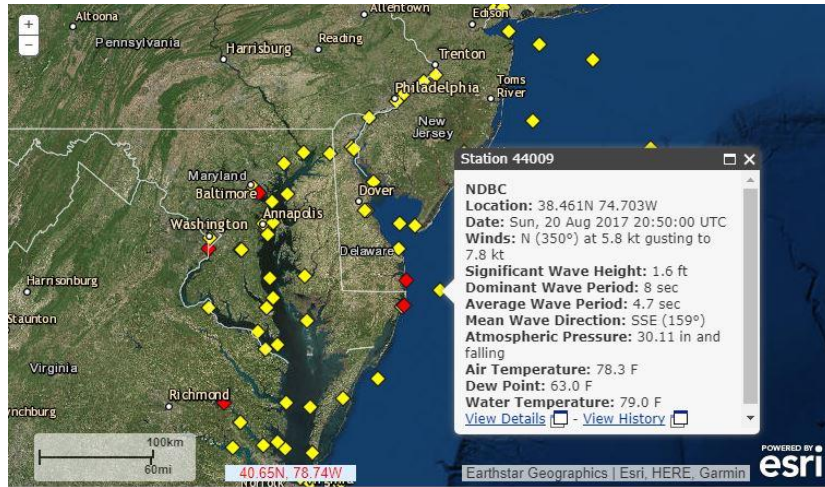


Fig. 6. Location of station 44009

The wind-wave misalignment angle is not directly given in the raw data. A modulo operation with respect to the wind and wave directions is performed to obtain the wind-wave misalignment angle. The misalignment range is chosen such that $-180^\circ \leq \beta \leq 180^\circ$.

Different statistical models have been tested to describe the distribution of the original data. It is found that the wind-wave misalignment, significant wave height and the wind speed can be satisfactorily represented by Gaussian, lognormal and Rayleigh distributions, respectively. Fig. 7 illustrates the comparison of the cumulative probability curve between the original data and the fitted curve where good agreement can be observed.

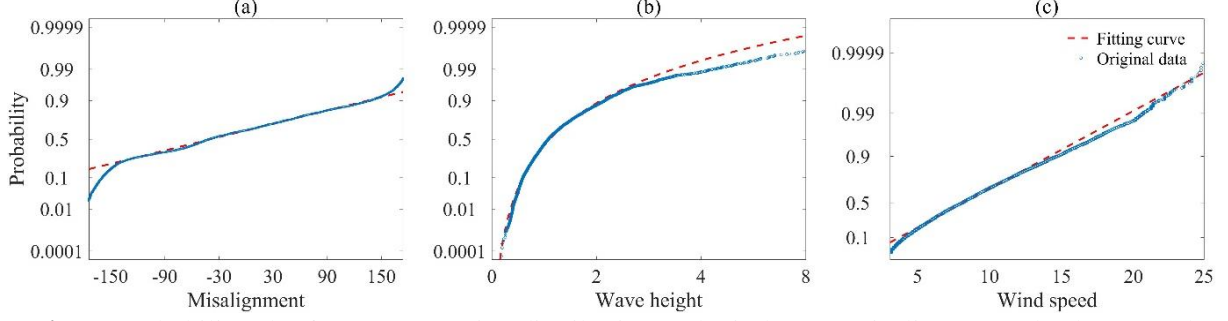


Fig. 7. Probability plot for: (a): Gaussian distribution and wind-wave misalignment; (b): lognormal distribution and significant wave height; (c): Rayleigh distribution and wind speed.

The joint probability for two independent random variables can be calculated as follows:

$$P((X_L < X < X_H) \cap (Y_L < Y < Y_H)) = [F_X(X_H) - F_X(X_L)] \times [F_Y(Y_H) - F_Y(Y_L)] \quad (33)$$

where P is the probability of occurrence. Parameters X and Y represent the random variables. Parameters X_L and X_H denote the lower and upper bounds of variable. F_X and F_Y are the cumulative distribution functions.

Since wind-wave misalignment is independent of the significant wave height and the wind speed, Eq. (33) can be applied to determine the joint probability function of wind-wave misalignment and the other two variables. Fig. 8(a) illustrates the contour plot of the joint probability of wind-wave misalignment and wind speed and Fig. 8(b) illustrates the contour plot of the joint probability of wind-wave misalignment and significant wave height.

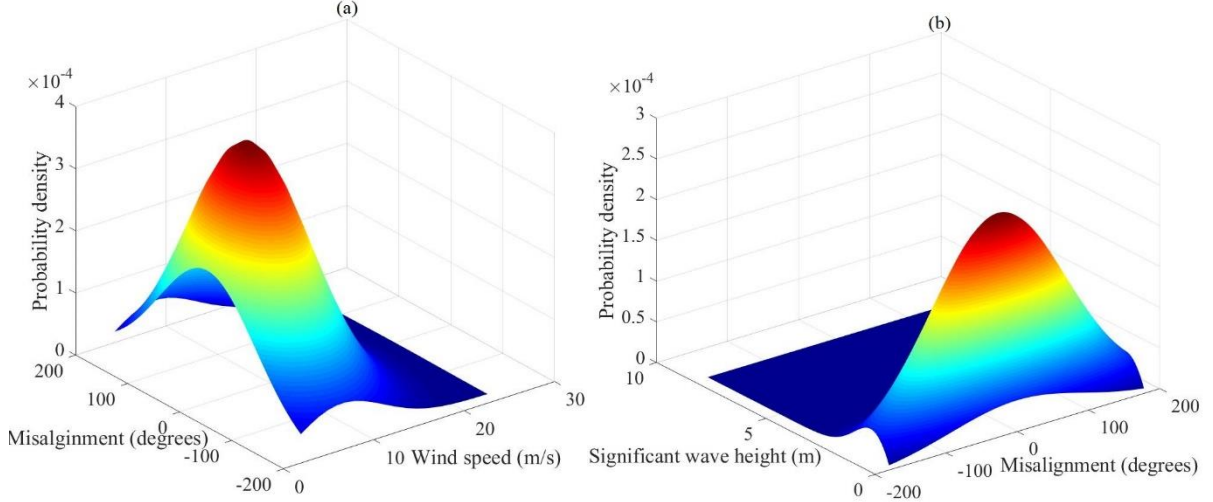


Fig. 8. Joint probability density for: (a): Wind speed–misalignment; (b): Significant wave height–misalignment

Wind speed and significant wave height are correlated random variables. Therefore, Eq. (33) is inapplicable to obtain the joint probability distribution of the two variables. As can be seen in Fig. 8 (a) and (b), the region corresponding to wind speed below 18 m/s and significant wave height below 4 m dominates the overall distribution. Thus, the joint probability of wind speed and significant wave height is determined for a truncated wind speed range from 3 m/s to 18 m/s and a truncated significant wave height range from 0 to 4 m. In this regard, the wind speed is divided

into 16 bins and the significant wave height is divided into 4 bins. The probability of occurrence for each bin is calculated and listed in Table 1. As an example, according to Table 1, the probability of occurrence for significant wave height from 1 m to 2 m and the wind speed from 8 m/s to 10 m/s is 13.4%.

Table. 1. Joint probability distribution of significant wave height and wind speed (%)

H_s	V								
	(4-6)	(6-8)	(8-10)	(10-12)	(12-14)	(14-16)	(16-18)	18	Total
1	13.52	15.6	13.4	9.6	4.6	1.4	1.1	0.05	59.27
2	2.52	3.46	4.3	5.4	6.3	5.9	3.8	1.4	33.08
3	0.24	0.4	0.5	0.7	1	1.39	1.3	0.76	6.29
4	0.02	0.03	0.07	0.1	0.2	0.3	0.43	0.21	1.36
Total	16.3	19.49	18.27	15.8	12.1	8.99	6.63	2.4	100

It should be noted that the wave period T is a random variable which is correlated with the significant wave height H_s . To provide insight into the correlation between T and H_s , histograms corresponding to different wave height (divided into 4 bins from 0 to 4m) are obtained and presented in Fig. 9 where the red line is the fitted curve of the histogram. Wave period at the peak of the fitted curve is taken as the dominant wave period of the given significant wave height range.

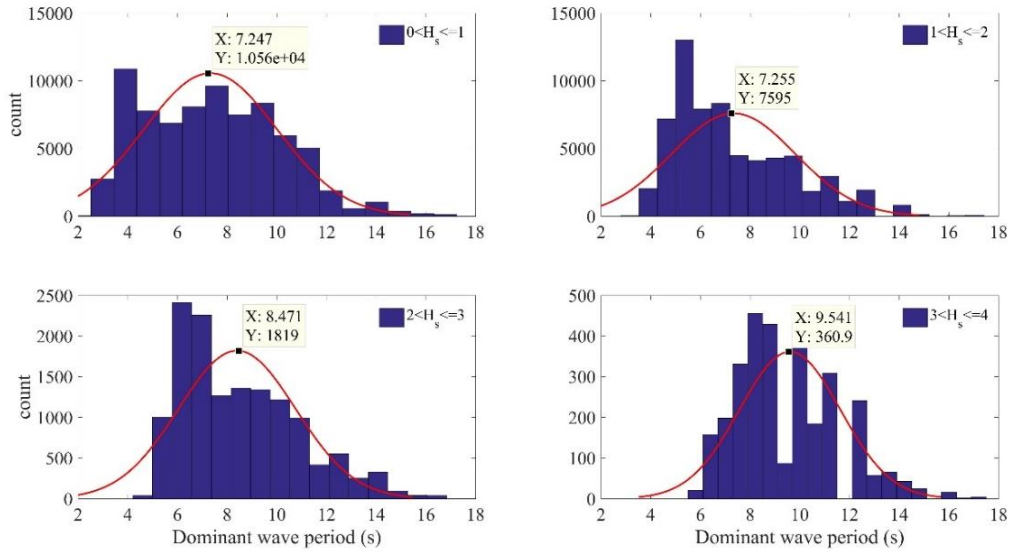


Fig. 9. Dominant wave period histogram in specific ranges of significant wave height

In summary, the metocean data is divided into 5 mean wind speed bins and 4 significant wave height bins with a fixed value of dominant wave period obtained from Fig. 9. To reduce the computational cost, 4 bins are considered for the wind-wave misalignment, namely 0° , 30° , 60° and 90° . Hence, 80 bins are considered totally. For each bin, simulation is conducted and the obtained structural response is used to estimate the wind-wave induced fatigue damage, which is presented in the following section.

6. Fatigue life estimation

This section estimates the fatigue life of the OWT tower under the recorded wind-wave conditions using the rain-flow cycle counting method. Two locations are selected for fatigue life estimation: the butt weld connection of the monopile foundation and the tower (referred to as S_1 in Fig. 1) and the butt weld connection of the monopile foundation and the seabed (referred to as S_2 in Fig. 1).

In the present study, the formula suggested by DNV [22] is used to evaluate the fatigue life:

$$\log_{10} N = \log_{10} a - m \log_{10} \left(\Delta \sigma \left(\frac{t}{t_{ref}} \right)^k \right) \quad (34)$$

where N is the number of cycles for the stress range of $\Delta \sigma$. Variable $\log_{10} a$ is the intercept of $\log_{10} N$ axis and m is the negative slope of S-N curve. Parameters t and t_{ref} are the plate and reference thickness respectively. Parameter k denotes an index parameter. With reference to [32], values of the parameters involved in Eq. (34) are chosen and listed as follows,

- a. For the atmospheric condition of the butt-welded connections [22]:

$$\log_{10} a = 12.164, m = 3$$

- b. For the undersea condition of the butt-welded connections [22]:

$$\log_{10} a = 11.674, m = 3$$

The reference thickness for tubular joints is 32 mm, and if the plate thickness is smaller than t_{ref} , $\frac{t}{t_{ref}}$ is equal to 1.

Total fatigue damage is calculated on the basis of the Miner's law expressed as:

$$D = \sum_i^N \frac{n_i}{N_i} \quad (35)$$

where n_i is the number of stress cycles in the i^{th} stress block and N_i is the number of cycles to failure at the design stress range of the i^{th} stress block.

As described in section 5, 80 loading conditions are considered in the present study. The mean wind velocity values at hub height are chosen as 6 m/s, 9 m/s, 12 m/s, 15 m/s and 18 m/s. Significant wave height and the dominant wave period are selected as 1 m and 7.3 sec, 2 m and 7.3 sec, 3 m and 8.5 sec, 4 m and 9.5 sec. Four representative wind-wave misalignment angles are used: 0°, 30°, 60° and 90°. The system is simulated under each loading condition and the associated fatigue damage is calculated using the rain-flow cycle counting method. The cumulative fatigue damage is calculated as follows:

$$D_{\text{total}} = \sum_{i=1}^{80} P_i D_i \quad (36)$$

where, P_i is the probability of each loading condition and D_i is the corresponding fatigue damage.

7. System Parameters

In this section, the associated parameter values of the baseline offshore wind turbine, the soil effects and loading parameters are presented. In the present study, the NREL 5MW OC3 monopile wind turbine model [23] is used. The parameters are listed in Table. 2. The edgewise and flapwise fundamental mode shapes of the blade and the tower are expressed as:

$$\begin{aligned}\phi_{1e}(\bar{r}) &= -0.6952\bar{r}^6 + 2.3760\bar{r}^5 - 3.5772\bar{r}^4 + 2.5337\bar{r}^3 + 0.3627\bar{r}^2 \\ \phi_{1f}(\bar{r}) &= -2.2555\bar{r}^6 + 4.7131\bar{r}^5 - 3.2452\bar{r}^4 + 1.7254\bar{r}^3 + 0.0622\bar{r}^2 \\ \phi_{1t}(\bar{h}) &= -0.6952\bar{h}^6 + 2.3760\bar{h}^5 - 3.5772\bar{h}^4 + 2.5337\bar{h}^3 + 0.3627\bar{h}^2\end{aligned}\quad (37)$$

where ϕ_{1e} and ϕ_{1f} denote the edgewise and flapwise fundamental mode shape of the blade; parameter ϕ_{1t} denotes the tower fore-aft and side-side fundamental mode shape. Variables $\bar{r} = r / 61.5$ and $\bar{h} = h / 87.6$ denote the normalized blade radius and tower height.

Table. 2. Parameters of the NREL 5-MW baseline wind turbine[23]

Gross	Rating	5 MW
	Rotor diameter	126 m
	Hub height	90 m
	Cut-in, rated, cut-out wind speed	3 m/s, 11.4 m/s, 25 m/s
	Cut-in, rated rotor speed	6.9 rpm, 12.1 rpm
Blade	Length	61.5 m
	Mass	17,740 kg
	Second moment of inertia	11,776 kgm ²
	1 st edgewise model natural frequency	1.08 Hz
	1 st flapwise model natural frequency	0.68 Hz
	1 st mode damping ratio	0.48%
Nacelle + hub	Nacelle mass	240,000 kg
	Hub mass	56,780 kg
	Hub diameter	3 m
Tower	Height above ground	87.6 m
	Overall mass	267,650 kg
	1 st fore-aft mode natural frequency	0.324 Hz
	1 st side-side mode natural frequency	0.312 Hz
	1 st fore-aft (side-side) modal damping	1%

The soil effect condition is considered via using linear springs and dash-pots. To represent the clay soil condition the spring stiffnesses are equal to, $k_x = k_y = 3.89E9 N / m$ and $k_{x\phi} = k_{y\phi} = 1.14E11 Nm / rad$. Also, the soil damping ratio are equal to $\xi_x = \xi_y = \xi_{x\phi} = \xi_{y\phi} = 0.6\%$ [24].

8. Results

In this section, the effectiveness of the 3d-PTMD in controlling the bi-directional vibration of the OWT is evaluated and the fatigue damage of the tower is determined.

The structural responses of the OWT are computed through numerically solving Eq. (10). The dual linear TMDs model studied in Ref. [12] is adopted for comparison. For a fair comparison, the frequency and damping ratio for the dual TMDs and 3d-PTMD is set to be equal. Based on [15], a suggested mass ratio of 2% is utilized and the corresponding optimal frequency ratio and damping ratio are: $f_{opt} = 0.97$ and $\xi_{opt} = 10\%$.

Structural response under all the selected wind-wave conditions are calculated for fatigue damage estimation. Due to paper length constraints, the bi-directional structural response corresponding to wind speed at hub height $v = 12m/s$ and significant wave height $H_s = 3m$ are illustrated as an example in Figs 10 and 11. In this paper, one realisation is used for each bin to estimate the fatigue damage since one realisation provides reasonable fatigue damage estimates based on [25].

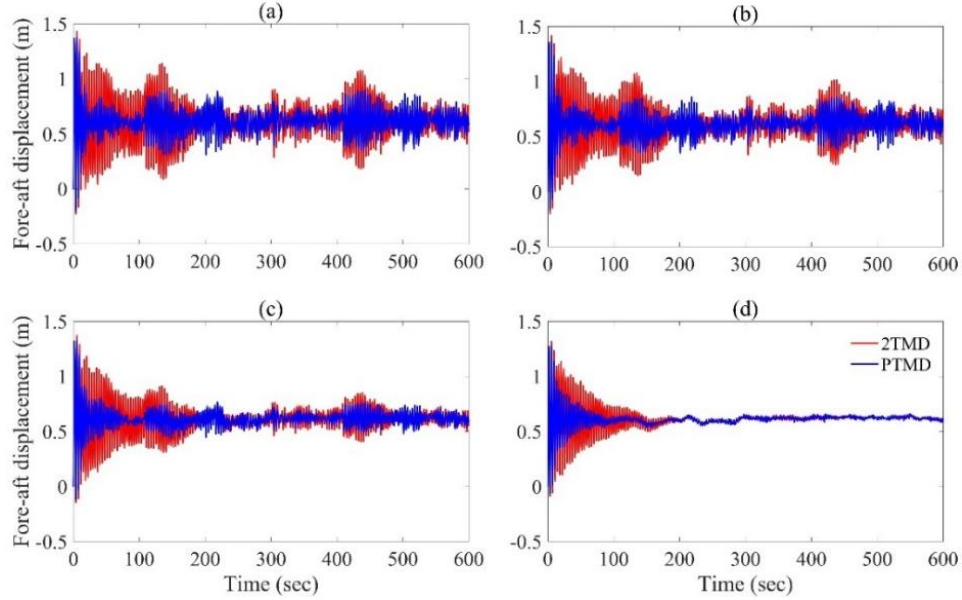


Fig. 10. Nacelle fore-aft displacement comparison between 3d-PTMD and dual TMDs for different wind-wave misalignment angles: (a): misalignment angle = 0° (b): misalignment angle = 30° (c): misalignment angle = 60° (d): misalignment angle = 90° .

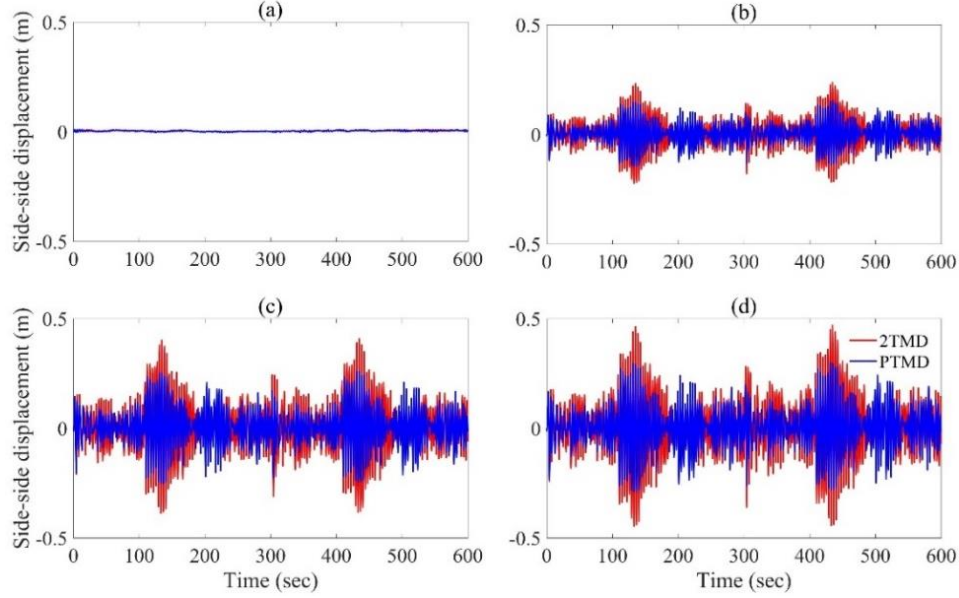


Fig. 11. Nacelle side-side displacement comparison between 3d-PTMD and dual TMDs for different wind-wave misalignment angles: (a): misalignment angle = 0° (b): misalignment angle = 30° (c): misalignment angle = 60° (d): misalignment angle = 90° .

Figs. 10 (a)-(d) show the nacelle fore-aft displacement time-history comparison between the dual TMDs and the 3d-PTMD under the four wind-wave misalignment angles. It can be found that the 3d-PTMD outperforms the dual TMDs in mitigating the nacelle response in the fore-aft direction. On top of that, Fig. 11 (a)-(d) indicate that the 3d-PTMD can mitigate the nacelle side-side response more effectively than the dual TMDs under different wind-wave misalignment. It should be noted that the side-side motion is minimal when the wind and wave loadings are aligned as shown in Fig. 11(a).

The bi-directional tower top displacement causes bi-directional bending moment M_x, M_y in the tower. The resultant stress distribution along the cross-section of the tower becomes complex due to the time-varying relative magnitude of the response in the fore-aft and side-side directions. Because of the symmetry of the cross section, six representative points (referred to as P_1 to P_6) evenly distributed along the out-most semi-circle of the tower cross-section are chosen for fatigue damage estimation. The representative points are illustrated in Fig. 12. The resultant stress of these chosen points are determined as:

$$\sigma_i = \frac{N_x}{A} + \frac{M_x}{I_x} r \sin \varphi_i - \frac{M_y}{I_y} r \cos \varphi_i \quad (38)$$

where N_x is the axial force, A is the nominal cross section area, M_x and M_y are the bending moments and I_x and I_y are the sectional moments of area.

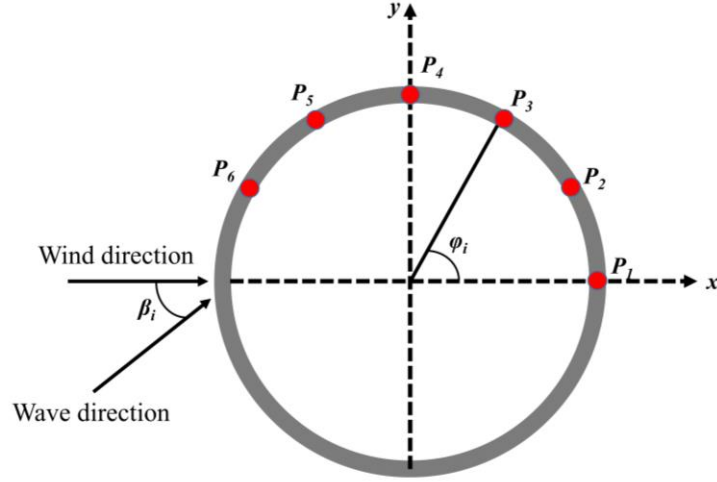


Fig. 12. Representative points distributed along the out-most semi-circle of the tower cross section.

Figs. 13 and 14 (a)-(d) demonstrate the stress time-history at P_1 and P_3 on the foundation-seabed cross section respectively. It can be seen that the 3d-PTMD reduces the stress more effectively than the dual TMDs. Also, it is found that the stress at P_1 is larger than the stress at P_3 .

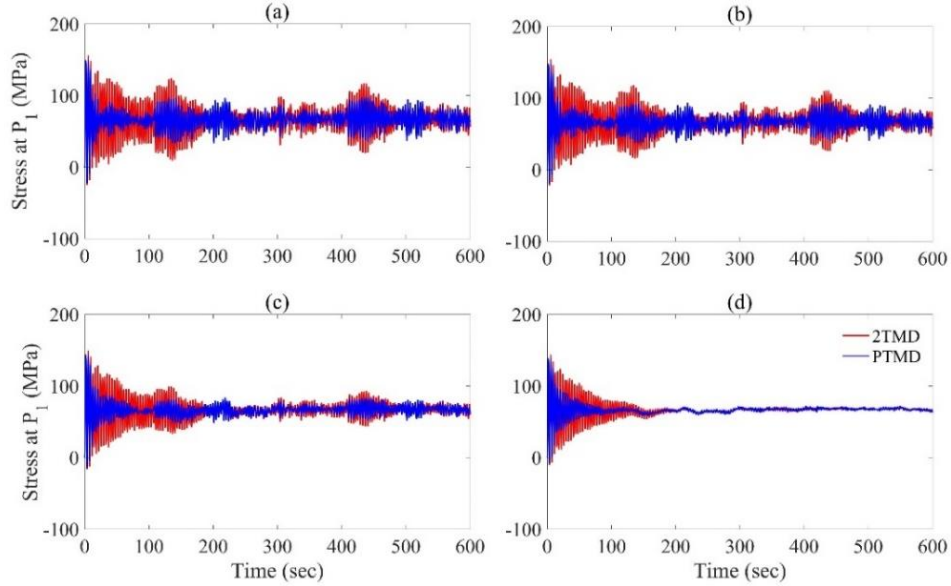


Fig. 13. Comparison of bending stress on foundation-seabed cross section at P_1 between 3d-PTMD and dual TMDs for different wind-wave misalignment angles: (a): misalignment angle = 0° ; (b): misalignment angle = 30° ; (c): misalignment angle = 60° ; (d): misalignment angle = 90° .

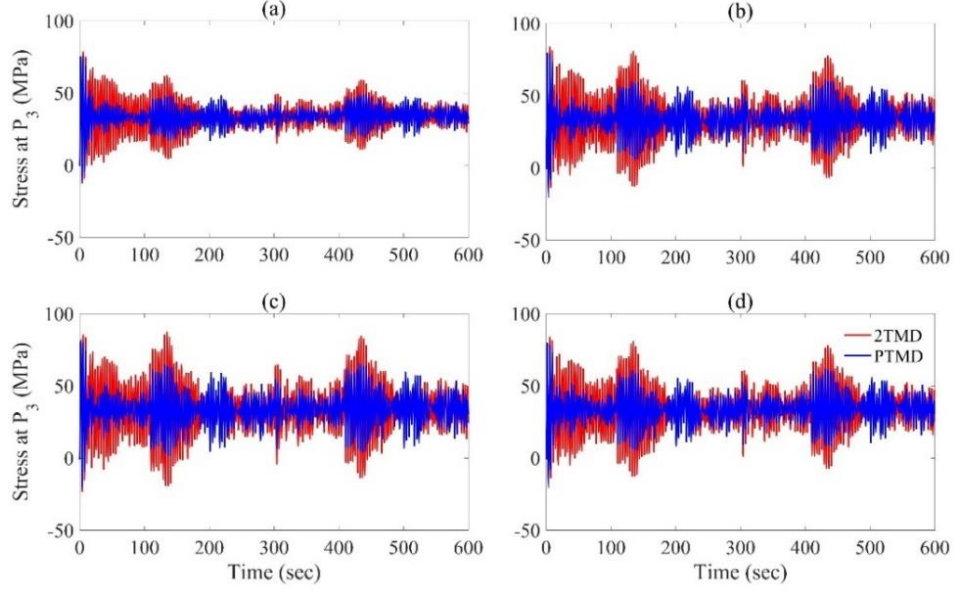


Fig. 14. Comparison of bending stress on foundation-seabed cross section at P_3 between 3d-PTMD and dual TMDs for different wind-wave misalignment angles: (a): misalignment angle = 0° ; (b): misalignment angle = 30° ; (c): misalignment angle = 60° ; (d): misalignment angle = 90° .

The rain-flow cycle counting method is applied to calculate the fatigue damage based on the stress time-history of each loading condition. The rain-flow matrix which shows the stress mean, stress amplitude and number of cycles corresponding to wind speed at hub height $v = 12 \text{ m/s}$ and significant wave height $H_s = 3 \text{ m}$ with misalignment angle of 30 degrees for P_1 and P_3 is illustrated in Figs. 15 and 16 (a) corresponding to the controlled wind turbine with 3d-PTMD and (b) corresponding to controlled wind turbine with dual TMDs for location P_1 of foundation-tower joint.

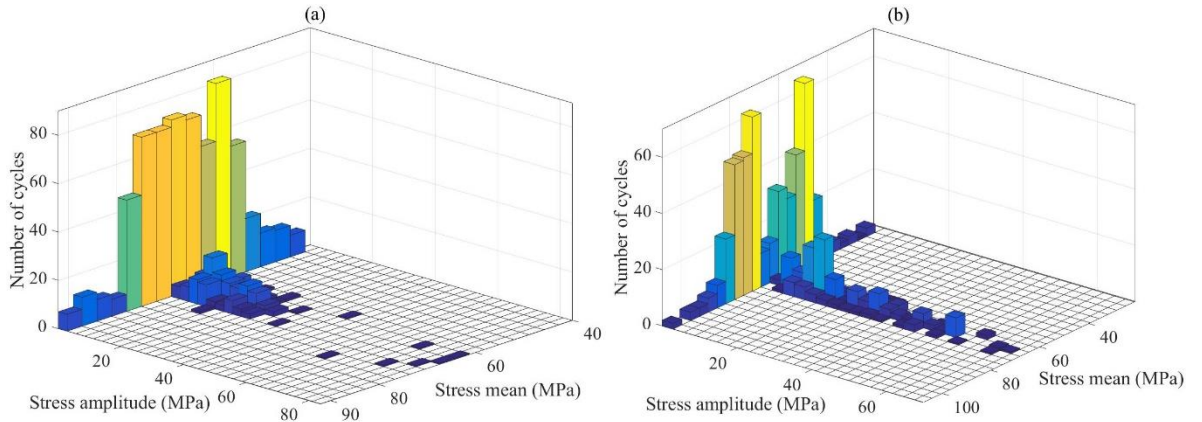


Fig. 15. Rain-flow matrix for P_1 : (a): 3d-PTMD (b): dual TMDs.

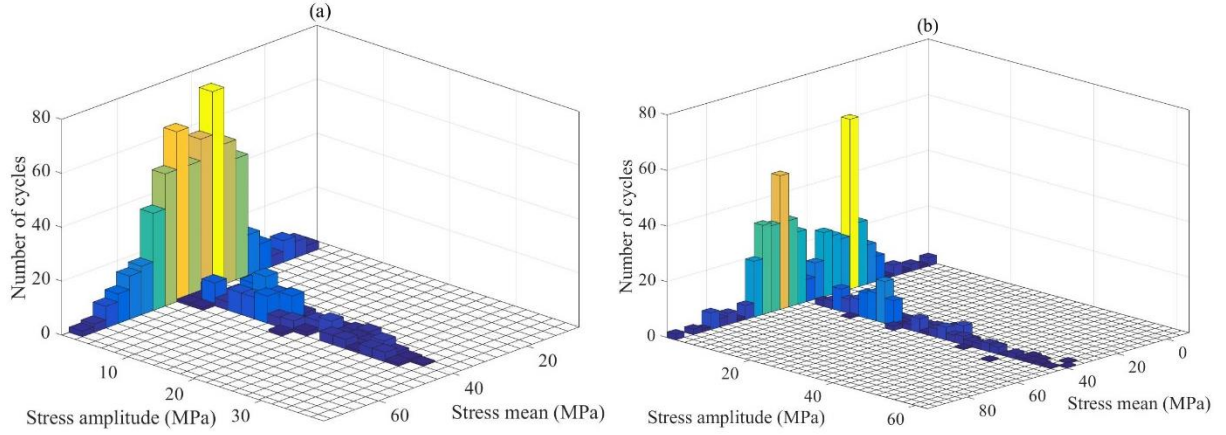


Fig. 16. Rain-flow matrix for P_3 : (a): 3d-PTMD (b): dual TMDs.

On the basis of the determined number of cycles and stress range, the cumulative fatigue damage of the 12 representative points under each of the loading conditions is calculated using the S-N curve and Miner's rule. Since the focus of the present study is to evaluate the performance of the 3d-PTMD in mitigating the fatigue damage, the cumulative fatigue damage of each point is determined using Eq. (38) within 600s rather than a longer window, e.g., 1 hour or 3 hours, to reduce the computational cost.

Table. 3. 600s cumulative fatigue damage with 3d-PTMD and dual TMDs

Location	Location in outer	Cumulative fatigue damage	
		3d-PTMD	2TMD
Foundation-tower	P ₁₁	1.0198	2.226
	P ₁₂	0.761	1.693
	P ₁₃	0.252	0.602
	P ₁₄	0.0679	0.1835
	P ₁₅	0.1397	0.3268
	P ₁₆	0.622	1.3616
Foundation-seabed	P ₂₁	1.4307	3.1231
	P ₂₂	1.067	2.3759
	P ₂₃	0.3544	0.8442
	P ₂₄	0.097	0.257
	P ₂₅	0.196	0.458
	P ₂₆	0.873	1.9102

To demonstrate the effectiveness of the 3d-PTMD, fatigue damage estimation of the tower controlled by the dual TMDs is also conducted for comparison. The final cumulative fatigue

damage results of the chosen 12 locations are listed in Table 3. It should be noted that P_{1i} is the representative points distributed along the out-most circle of the foundation-tower cross section and P_{2i} is the representative points distributed along the out-most circle of the foundation-seabed cross section.

Table 3 indicates that on the foundation-tower cross section, the cumulative fatigue damage gradually decreases from P_{11} to P_{14} and then gradually increases till P_{16} . Similar conclusion can be obtained on the foundation-seabed cross section. In comparison with the dual TMDs, one can find that the 3d-PTMD can mitigate the fatigue damage up to 50% for both the foundation-tower and foundation-seabed cross sections. Furthermore, it can be seen that the fatigue damage of the foundation-seabed cross section is higher than that of the foundation-tower cross section because the former experiences higher stress cycles than the latter.

9. Conclusion

Fatigue damage caused failure is a dominant failure mechanism for offshore wind turbines. In the present study, mitigation of fatigue damage of the monopile offshore wind turbines to be constructed at the specified location is studied using a 3d-PTMD under real metocean conditions. A fully coupled three dimensional analytical model of the OWT with the 3d-PTMD is utilized. Statistical analysis of the recorded wind and wave data is conducted to obtain the key probabilistic distribution parameter values used to generate wind-wave loading as well as to estimate the long-term fatigue damage. Using the rain-flow cycle counting method, the fatigue damage of the tower is estimated and compared between the case with a 3d-PTMD and that with dual linear TMDs. Based on the presented results and discussions, the following conclusions can be obtained:

- 1- A statistical analysis is conducted with respect to the recorded wind and wave data from the station 44009 where a new offshore wind farm (with monopile offshore wind turbines) is under planning. The statistical characteristics of the wind wave data including the wind speed, wave period, significant wave height and wind-wave misalignment are obtained. The obtained statistical results are not only critical for fatigue damage estimation in the present study, but also significantly valuable for further analysis and design of the monopile OWTs to be constructed.
- 2- Total fatigue damage within ten minutes is calculated via cumulating the fatigue damage caused by wind-wave loading from each bin considering their probability. It is indicated that in comparison with the dual TMDs, the 3d-PTMD can mitigate the fatigue damage up to 50%. In other words, the fatigue life of the OWT tower will be prolonged by more than 50 percent using the 3d-PTMD than using the dual TMDs.
- 3- The fatigue damage in the butt weld connection of the monopile foundation and the seabed is higher than that of the connection of the monopile foundation and the tower.
- 4- The fatigue damage at locations P_{11} and P_{21} of the out-most circle of the tower cross section is higher than any other locations of the tower-foundation and foundation-seabed cross sections. This provides valuable practical guidance for analysis and design of OWTs to be constructed in the new wind farm.

Acknowledgment

This work was supported by Louisiana State University Start-up Fund (fund number is 127150013), the Faculty Research Grant (fund number is 127159132) and the Innovation in Engineering Research (FIRE) Grant provided by the College of Engineering at Louisiana State

University. This work was also supported by the National Natural Science Foundation of China (51679167). The authors are grateful for all the support.

References

- [1] Colwell S, Basu B. Tuned liquid column dampers in offshore wind turbines for structural control. *Eng Struct* 2009;31:358–68. doi:10.1016/j.engstruct.2008.09.001.
- [2] Lackner MA, Rotea MA. Passive structural control of offshore wind turbines. *Wind Energy* 2011;14:373–88. doi:10.1002/we.426.
- [3] Dinh V-N, Basu B. Passive control of floating offshore wind turbine nacelle and spar vibrations by multiple tuned mass dampers. *Struct Control Heal Monit* 2015;22:152–76. doi:10.1002/stc.1666.
- [4] Lackner MA, Rotea MA. Structural control of floating wind turbines. *Mechatronics* 2011;21:704–19. doi:10.1016/j.mechatronics.2010.11.007.
- [5] Staino A, Basu B, Nielsen SRK. Actuator control of edgewise vibrations in wind turbine blades. *J Sound Vib* 2012;331:1233–56. doi:10.1016/j.jsv.2011.11.003.
- [6] Fitzgerald B, Basu B. Cable connected active tuned mass dampers for control of in-plane vibrations of wind turbine blades. *J Sound Vib* 2014;333:5980–6004. doi:10.1016/j.jsv.2014.05.031.
- [7] Sun C. Semi-active control of monopile offshore wind turbines under multi-hazards. *Mech Syst Signal Process* 2018;99:285–305. doi:10.1016/j.ymssp.2017.06.016.
- [8] Sun C. Mitigation of offshore wind turbine responses under wind and wave loading: Considering soil effects and damage. *Struct Control Heal Monit* 2018;25:e2117. doi:10.1002/stc.2117.
- [9] Huang C, Arrigan J, Nagarajaiah S, Basu B. Semi-Active Algorithm for Edgewise Vibration Control in Floating Wind Turbine Blades. *Earth Sp.* 2010, Reston, VA: American Society of Civil Engineers; 2010, p. 2097–110. doi:10.1061/41096(366)192.
- [10] Arrigan J, Pakrashi V, Basu B, Nagarajaiah S. Control of flapwise vibrations in wind turbine blades using semi-active tuned mass dampers. *Struct Control Heal Monit* 2011;18:840–51. doi:10.1002/stc.404.
- [11] Dinh V-N, Basu B, Nagarajaiah S. Semi - Active Control of Vibrations of Spar Type Floating Offshore Wind Turbines. *Smart Struct Syst* 2016;18:683–705. doi:10.12989/sss.2016.18.4.683.
- [12] Stewart GM, Lackner MA. The impact of passive tuned mass dampers and wind–wave misalignment on offshore wind turbine loads. *Eng Struct* 2014;73:54–61. doi:10.1016/j.engstruct.2014.04.045.
- [13] Sun C, Nagarajaiah S, Dick AJ. Family of smart tuned mass dampers with variable frequency under harmonic excitations and ground motions : closed - form evaluation. *Smart Struct Syst* 2014;13:319–41. doi:10.12989/sss.2014.13.2.319.
- [14] Sun C, Nagarajaiah S, Dick AJ. Experimental investigation of vibration attenuation using nonlinear tuned mass damper and pendulum tuned mass damper in parallel. *Nonlinear Dyn*

- 2014;78:2699–715. doi:10.1007/s11071-014-1619-3.
- [15] Sun C, Jahangiri V. Bi-directional vibration control of offshore wind turbines using a 3D pendulum tuned mass damper. *Mech Syst Signal Process* 2018;105:338–60. doi:10.1016/j.ymssp.2017.12.011.
 - [16] Skipjack Wind Farm Request for Proposals – Environmental Analysis and Permitting Support. 2017.
 - [17] Jonkman BJ, Kilcher L. TurbSim User’s Guide: Version 1.06.00 DRAFT VERSION 2012.
 - [18] Hansen MOL. Aerodynamics of wind turbines. Earthscan; 2008.
 - [19] Faltinsen OM (Odd M. Sea loads on ships and offshore structures. Cambridge University Press; 1993.
 - [20] IEC - Part 3: Design requirements for offshore wind turbines (IEC 61400-3:2009): METROLOGY AND TESTING CZECH OFFICE FOR STANDARDS: 8590963839257: Amazon.com: Books. Geneva, Switzerland: 2009.
 - [21] US Department of Commerce NO and AANWSNDBC. National Data Buoy Center n.d.
 - [22] Norske Veritas D. DET NORSKE VERITAS AS Design of Offshore Wind Turbine Structures 2014.
 - [23] Jonkman J, Butterfield S, Musial W, Scott G. Definition of a 5-MW Reference Wind Turbine for Offshore System Development 2009.
 - [24] Carswell W, Johansson J, Løvholt F, Arwade SR, Madshus C, Degroot DJ, et al. Foundation damping and the dynamics of offshore wind turbine monopiles. *Renew Energy* 2015;80:724–36. doi:10.1016/j.renene.2015.02.058.
 - [25] Kvittem MI, Moan T. Time domain analysis procedures for fatigue assessment of a semi-submersible wind turbine. *Mar Struct* 2015;40:38–59. doi:10.1016/J.MARSTRUC.2014.10.009.